International Journal of Coal Science & Technology (2024) 11:45
https://doi.org/10.1007/s40789-024-00697-7

RESEARCH

Screening the optimal $Co_x/CeO_2(110)$ ($x = 1–6$) catalyst for methane activation in coalbed gas

Li'nan Huang[1,2] · **Danyang Li**[1,2] · **Lei Jiang**[1,2] · **Zhiqiang Li**[1,2] · **Dong Tian**[1,2,3] · **Kongzhai Li**[1,2,3]

Received: 1 September 2023 / Revised: 11 October 2023 / Accepted: 25 April 2024

Abstract

The challenges posed by energy and environmental issues have forced mankind to explore and utilize unconventional energy sources. It is imperative to convert the abundant coalbed gas (CBG) into high value-added products, i.e., selective and efficient conversion of methane from CBG. Methane activation, known as the "holy grail", poses a challenge to the design and development of catalysts. The structural complexity of the active metal on the carrier is of particular concern. In this work, we have studied the nucleation growth of small Co clusters (up to Co_6) on the surface of $CeO_2(110)$ using density functional theory, from which a stable loaded $Co/CeO_2(110)$ structure was selected to investigate the methane activation mechanism. Despite the relatively small size of the selected Co clusters, the obtained $Co_x/CeO_2(110)$ exhibits interesting properties. The optimized $Co_5/CeO_2(110)$ structure was selected as the optimal structure to study the activation mechanism of methane due to its competitive electronic structure, adsorption energy and binding energy. The energy barriers for the stepwise dissociation of methane to form CH_3*, CH_2*, CH*, and C* radical fragments are 0.44, 0.55, 0.31, and 1.20 eV, respectively, indicating that CH* dissociative dehydrogenation is the rate-determining step for the system under investigation here. This fundamental study of metal-support interactions based on Co growth on the $CeO_2(110)$ surface contributes to the understanding of the essence of Co/CeO_2 catalysts with promising catalytic behavior. It provides theoretical guidance for better designing the optimal Co/CeO_2 catalyst for tailored catalytic reactions.

Keywords Co cluster growth · Ce-based catalysts · Methane activation · DFT

1 Introduction

The advantages of developing renewable energy are obvious, since the issues of energy, environment, and climate change brought about by the rapid development of the world economy have become prominent global challenges today (Huang et al. 2022; Wu et al. 2022, 2023). Coalbed gas (CBG), mainly composed of methane (30% to more than 95% (Zhang et al. 2016), is a reserve-rich unconventional natural gas resource with buried between coal seams, which is expected to play an important role in the future energy portfolio (Ma et al. 2022; Mastalerz and Drobniak 2020). In recent years, methane from CBG has been utilized or converted into high value-added products through a range of means, all of which include fuel cells (Yang et al. 2022a, b), dry reforming of methane (Yang et al. 2023; Zhang et al. 2004), and partial oxidation (Chang et al. 2023; Sedov et al. 2022), has become a focus of attention. As a result of the high symmetry of the methane structure, the selective activation of its C-H bonds has been regarded as the "holy grail" of catalysis (Meng et al. 2019), which typically requires harsh conditions to efficiently cleave the four strongly localized C-H bonds with a bond energy of 439 kJ/mol. Therefore, it is the focus and challenge of current studies to develop new

✉ Dong Tian
dong.tian@aliyun.com; dong.tian@kust.edu.cn

✉ Kongzhai Li
kongzhai.li@aliyun.com; kongzhai.li@foxmail.com

[1] Engineering Research Center of Metallurgical Energy Conservation and Emission Reduction, Ministry of Education, Kunming University of Science and Technology, Kunming 650093, China

[2] Faculty of Metallurgical and Energy Engineering, Kunming University of Science and Technology, Kunming 650093, China

[3] State Key Laboratory of Complex Nonferrous Metal Resources Clean Utilization, Kunming University of Science and Technology, Kunming 650093, China

catalysts capable of selectively and efficiently converting and utilizing methane from CGB.

The oxide MOs of transition group metals M (M = Mo, V, Fe, Co and Cu) have been employed for the selective conversion of CH_4 because of their unique activity and selectivity (Ravi et al. 2017). The Co-based catalysts have demonstrated an excellent activity in catalyzing combustion of methane, partial oxidation of methane to methanol or syngas, as well as oxidative coupling of methane (Taylor et al. 1998; Zhang et al. 2005). In our previous study, a bifunctional material (Co_3O_4/(SiAl@Al_2O_3) coupled with a catalytic component (Co_3O_4) and a phase-change heat-storage component (SiAl@Al_2O_3) was firstly applied to the catalytic combustion of lean methane (Li et al. 2020). Mousavian and Esrafili (2020) found that the Co-modified $C_{24}N_{24}$ fullerene had excellent catalytic activity towards CH_4 oxidation to CH_3OH by theoretical calculations, and the reactive electron energy barrier of the $CH_4 + O_{ads} \rightarrow CH_3OH$ process on Co@$C_{24}N_{24}$ was only 0.60 eV. Blankenship et al. (2021) achieved high yields of methane aerobic conversion to the antioxidant methyl ester under moderate temperatures and pressures using highly dispersed cobalt-containing solid catalysts. Their work claimed that the cobalt-based catalyst had the most competitive activity (conversion and yield) versus any of the known transition metal aerobic catalytic systems. The reaction of cobalt pre-catalysts with methane and longer alkane congeners has been reported to require the passage of oxygen species (Strassner et al. 2013), while cerium dioxide, an important rare earth oxide, is widely used as a multiphase catalyst, fuel cell and biomedical material due to its excellent oxidation-reduction and oxidation-storage capacity (Cheng et al. 2021; Montini et al. 2016; Wu et al. 2021). Li and co-workers (Li et al. 2019) investigated a mechanism for ethanol steam reforming (ESR) reaction using density functional theory for Co_{13}/CeO_{2-x} configuration. Their studies showed that the ESR process depended on the valence state of the Co sites, specifically, maintaining a higher Co^0/Co^{2+} ratio resulted in a higher proportion of Co^0 and Co^{x+} sites, which helped to improve the ESR activity. The significance of metal-oxide interactions for the activation of methane over powdered cobalt dioxide-cerium dioxide catalysts was emphasized by Zhang et al. who immobilized Co on the cerium surface and used the redox nature of CeO_2 to activate methane (Zhang et al. 2018).

The synergistic effect between cobalt and cerium is essential for the successful completion of the catalytic process, significantly improving catalytic reactivity and stability (Liu et al. 2019). It has been reported by Zhou et al. (2021) that Co tends to cover the surface of $CeO_{1.96}$ with a monolayer structure at very low Co coverage to form a Co-O-Ce structure under room temperature, and the particles grow into a three-dimensional structure as the Co coverage increases. In addition, they found that the cobalt on Co/CeO_2 catalysts exhibited high thermal stability and highly dispersed small particle size due to the strong metal-support interaction of Co with ceria. Cerium dioxide can alter the electronic properties and oxygenophilicity of Co (Martono and Vohs 2012; Vovchok et al. 2018; Zhang et al. 2018). The chemistry of cobalt on cerium dioxide was very different from that of bulk cobalt because cobalt can form on cerium dioxide in metallic and oxidized states, which play different roles in chemical reactions (Zhang et al. 2018). In addition, metal/metal-oxide clusters have received increasing attention for their size-related properties as a key facilitator of heterogeneous catalytic processes (Zheng et al. 2022). Therefore, it is necessary to obtain physical information about Co-Ce catalysts using computational simulations to understand their detailed structures, chemical states and interactions.

Here, a systematic study of the growth pattern of small ($x = 1 \sim 6$) Co_x clusters on the surface of CeO_2(110) was performed using density functional theory. The focus was placed on the structure, electronic information, and metal-support interactions of the loaded Co_x/CeO_2(110) surface. Furthermore, the mechanism of activating methane on the optimal Co_5/CeO_2(110) configuration is highlighted. This fundamental study of Co growth on the CeO_2(110) surface, which contributed to the understanding of its promising catalytic behavior, provided theoretical guidance for the improved design of optimal Co/CeO_2 catalysts for tailored catalytic reactions.

2 Computational methods and details

All spin polarized Density Functional Theory (DFT) calculations in this study were performed using the first-principles calculations as implemented in the $DMol^3$ code (Delley 2000). The generalized gradient approximation (GGA) (Perdew et al. 1996) Perdew-Burke-Ernzerhof potential for solids (PBEsol) (Perdew et al. 2008) functional was used to calculate the exchange and correlation energies. The following electrons were treated as valence electrons: Ce-5s, 5p, 5d, 4f, and 6s; Co-4s, 4p, and 3d; C-2s and 2p; H-1s; O-2s and 2p (Liu et al. 2017; Tian et al. 2018). The adsorption properties were calculated using the spin-unrestricted approach (Delley 1990). Added a dual-numeric basis set (version 4.4) (Delley 2006; Kumari et al. 2015) with orbital polarization for molecular orbitals (Delley 1990). The global orbital cut-off was set to 5.8 Å (Tian et al. 2018). The interactions between ions and electrons were described using the DFT semi-core pseudopotential (DSPP) (Kumari et al. 2015). The convergence criteria for the optimization of all structural configurations were the atomic force threshold of 2.0×10^{-3} Hartree/Å, the maximum displacement of 5.0×10^{-3} Å, the total energy change of 1.0×10^{-5} Hartree, and the self-consistent field (SCF) of 1.0×10^{-6} Hartree. Brillouin zone integrations were performed on the CeO$_2$ bulk and CeO$_2$(110) surfaces with 6×6×6 and 2×2×1 Monkhorst-Pack grids, respectively. The bulk lattice parameters of CeO$_2$ crystal was calculated to be $a = b = c = 5.421$ Å, which was well consistent with the previous calculations ($a = b = c = 5.423$ Å from Ref. (Tian et al. 2017, 2018) and experimental results ($a = b = c = 5.410$ Å from Ref. (Adachi and Imanaka 1998). This indicates that the calculation methodology used in this work is reliable.

Among the three low Miller index surfaces of CeO$_2$, the (111) surface is the most stable, the (110) surface is the second most stable, and the (100) surface is the least stable (Tian et al. 2017). The catalytic activity of CeO$_2$(110) surface is always considered to be higher than that of (111) and (100) surfaces, so it was chosen to investigate the reaction mechanism (Chutia et al. 2018; Tian et al. 2017; Zhou et al. 2022). As recently reported by Qu et al. (2022) that the Ru-loaded CeO$_2$(110) configuration is extremely competitive for the first C-H bond dissociation of methane compared to CeO$_2$(111). Therefore, we selected (110) surface to study the growth characteristics of Co$_x$ ($x = 1 \sim 6$) and investigated the CH$_4$ activation mechanism on the optimal Co/CeO$_2$(110) model. The CeO$_2$(110) surface was a model of an optimized CeO$_2$ bulk primitive cell cut and expanded to $2 \times \sqrt{10}$ with four atomic layers, the bottom two being fixed. 15 Å vacuum layer was used to avoid unphysical interactions of the model due to periodic mirroring. For the calculations of the CH$_4$*, CH$_3$*, CH$_2$*, CH*, C*, H$_2$*, O$_2$* and Co$_x$ ($x = 1 \sim 6$) cluster, the $(10 \times 10 \times 10)$ Å^3 box was used.

To mimic the growth structure of clusters, Co$_x$ ($x = 1 \sim 6$) were optimized by random placement on CeO$_2$(110) surfaces. However, the number of possible geometries becomes too numerous to be fully considered as the size of the Co clusters increases. Thus, we acquired Co clusters from the face-centered cubic structure relying on the findings of Datta and Ma et al. (Datta et al. 2007; Ma et al. 2006) to determine their geometry. We maintain that the clusters obtained are unquestionably representative, although this approach may not necessarily yield the most stable Co$_x$ clusters. The initial adsorption model for Co$_x$ ($x = 1 \sim 6$) clusters was shown in Fig. S1. Co$_1$ and Co$_2$ had only one initial structure, while examining Co$_3$, we focused on the planar triangular (Co$_{3-\mathrm{p}}$) model as the initial adsorption configuration rather than the linear model (Co$_{3-\mathrm{l}}$) due to the triangular structure of Co$_3$ being more energetically stable (Datta et al. 2007). There were two kinds of structures in Co$_4$ without considering linear structure: planar rhombohedral structure, Co$_{4-\mathrm{p}}$, and spatial tetrahedral structure, Co$_{4-\mathrm{t}}$. Because of the unique structure of Co$_4$, exploring the optimal adsorption structure of Co$_4$ is the key to investigating the growth mode of Co$_x$ on the surface of CeO$_2$(110) (surface tiling or three-dimensional clusters). According to the optimal adsorption structure of Co$_4$, we investigated the adsorption of stereo-structured Co$_5$ and Co$_6$ on CeO$_2$(110) surface. Nearly all of the possible clustering sites for Co$_x$($x = 1$–6) have been considered on the surface of CeO$_2$(110) according to the model we have constructed (see Supplementary material).

In this work, the adsorption energy ($\mathrm{E}^{\mathrm{ads}}_{\mathrm{Co}_x}$) of Co$_x$($x = 1$–6) on CeO$_2$ (110) surface in the growth study was obtained from the following equation:

$$\mathrm{E}^{\mathrm{ads}}_{\mathrm{Co}_x} = \mathrm{E}_{\mathrm{Co}_x/\mathrm{CeO}_2(110)} - \left(\mathrm{E}_{\mathrm{Co}_x} + \mathrm{E}_{\mathrm{CeO}_2(110)}\right) \tag{1}$$

where $\mathrm{E}_{\mathrm{Co}_x/\mathrm{CeO}_2(110)}$, $\mathrm{E}_{\mathrm{Co}_x}$ and $\mathrm{E}_{\mathrm{CeO}_2(110)}$ is represent the energies of the system after adsorption of Co$_x$ clusters on the CeO$_2$(110) surface, Co$_x$ cluster and CeO$_2$(110) surface, respectively.

Similarly, the adsorption energy ($\mathrm{E}^{\mathrm{ads}}_{\mathrm{CH}_4}$) of CH$_4$ on Co$_x$/CeO$_2$(110) model can be obtained:

$$\mathrm{E}^{\mathrm{ads}}_{\mathrm{CH}_4} = \mathrm{E}_{\mathrm{CH}_4\text{-}\mathrm{Co}_x/\mathrm{CeO}_2(110)} - \left(\mathrm{E}_{\mathrm{CH}_4} + \mathrm{E}_{\mathrm{Co}_x/\mathrm{CeO}_2(110)}\right) \tag{2}$$

where $\mathrm{E}_{\mathrm{CH}_4\text{-}\mathrm{Co}_x/\mathrm{CeO}_2(110)}$ is the energy of the system after adsorption of CH$_4$ on the optimal Co$_x$/CeO$_2$(110) model, and $\mathrm{E}_{\mathrm{CH}_4}$ is energy of methane in the gas phase. The adsorption energies of CH$_3$* and H* species are calculated with reference to $\mathrm{E}^{\mathrm{ads}}_{\mathrm{CH}_4}$.

The binding energy (E$_\mathrm{B}$) of per Co atom in the Co$_x$/CeO$_2$(110) ($x = 2 \sim 4$) model was defined as

$$\mathrm{E}_\mathrm{B} = \left(\mathrm{E}_{\mathrm{Co}_x/\mathrm{CeO}_2(110)} - x\mathrm{E}_{\mathrm{Co}} - \mathrm{E}_{\mathrm{CeO}_2(110)}\right)/x \tag{3}$$

where E_{Co} represent the energies of a single Co atom. Binding energy was used to characterize the stability of the structure (negative value, exothermic, stable; positive value, endothermic, unstable).

In the Co$_x$/CeO$_2$(110) model, the E$_\mathrm{B}$ is contributed by metal-substrate and metal-metal interactions. The metal-metal cohesive energy (E$_{\mathrm{Co-Co}}$, in eV per Co atom) and the metal-substrate adhesion energy (E$_{\mathrm{Co-O(Ce)}}$, in eV per Co atom) were derived from the following equations, respectively:

$$\mathrm{E}_{\mathrm{Co\text{-}Co}} = \left(\mathrm{E}_{\mathrm{Co}_x} - x\mathrm{E}_{\mathrm{Co}}\right)/x \tag{4}$$

$$\mathrm{E}_{\mathrm{Co-O(Ce)}} = \mathrm{E}_\mathrm{B} - \mathrm{E}_{\mathrm{Co-Co}} = \left(\mathrm{E}_{\mathrm{Co}_x/\mathrm{CeO}_2(110)} - \mathrm{E}_{\mathrm{Co}_x} - \mathrm{E}_{\mathrm{CeO}_2(110)}\right)/x \quad (5).$$

The growth structure of cobalt clusters on the CeO$_2$(110) surface can be determined by comparing E$_{\mathrm{Co-Co}}$ and

$E_{Co-O(Ce)}$. The former has to be more negative than the latter to form clusters, and vice versa.

The linear synchronous transition/quadratic synchronous transition (LST/QST) method (Halgren and Lipscomb 1977) with conjugate gradient minimization was used to search for the transition states (TS) of each radical reaction during the complete dissociation of methane. The root mean square (RMS) force on the transition state was optimized to be less than 5.25 kJ/mol·Å. The vibrational frequency analysis confirmed that the transition state structure has one and only one imaginary frequency. The activation energy barrier (E_a) and the reaction energy (E_{re}) of the radical reaction were calculated by the formulas given in the following equations:

$E_a=E_{TS}-E_{IS}$ (6).

$E_{re}=E_{FS}-E_{IS}$ (7).

where E_{TS}, E_{IS} and E_{FS} are the total electron energies of the TS, initial state (IS) and final state (FS), respectively.

3 Results and discussions

3.1 Growth pattern of Co_x ($x = 1 \sim 6$) on $CeO_2(110)$ surface

Six initial adsorption sites for the adsorption of monoatomic Co on the $CeO_2(110)$ surface were considered, which included Ce top site (Ce-top), O top site (O-top), double oxygen bridge site (Double-O-br) and three different oxygen bridge sites (O-br (1), O-br (2), O-br (3), see Fig. S2. Three stable adsorption sites were formed after the relaxation of the $Co_1/CeO_2(110)$ structure, shown in Fig. 1, with respective adsorption energies of -6.10, -4.69, and -7.13 eV. The double-O-br site was the most stable adsorption site for Co_1 on the $CeO_2(110)$ surface, which was consistent with that of Ni_1 (Li et al. 2016). The Co adsorption energy was stronger in $CeO_2(110)$ than in $CeO_2(111)$ (-4.89 eV) (Tian et al. 2018). Table 1 summarized the bond length information of the stable structure of $Co_x/CeO_2(110)$. The Co-O bond lengths in the $Co_1/CeO_2(110)$ structure with Co adsorbed at the double O-br site were 3 × 1.85 Å and 1.84 Å, respectively, which are smaller than the experimentally reported $R_{Co-O}(CoO) = 2.14$ Å and $R_{Co-O}(Co/CeO_2) = 1.97$ Å by Deng et al. (2020). The distance d_{Ce-O}= 2.68 Å between surface O and subsurface Ce is greater than the standard value of 2.35 Å indicates that surface O is more active. In addition, the Mulliken charge analysis showed that isolated Co atom was transferred 0.44 e to the support, resulting in the reduction of two Ce^{4+} to Ce^{3+}.

Thirteen initial adsorption configurations (Fig. S3) of Co_2 on the surface of $CeO_2(110)$ resulted in six stable $Co_2/CeO_2(110)$ configurations (Fig. 2) after surface relaxation. The adsorption models for Co_2-(a, c, d, f, g) sites and Co_2-(b, e, l, m) sites were geometrically optimized to form the stable adsorption configurations of Co_2-a (Fig. 2b) and Co_2-b (Fig. 2c), respectively. Co_2-h, Co_2-i, Co_2-j and Co_2-k (Figs. 2d-g) form independent adsorption configurations, where Co_2-h and Co_2-k were not reasonable adsorption structures for $Co_2/CeO_2(110)$ because the Co-Co distance was too far here (3.99 and 5.50 Å). The most stable adsorption configuration of Co_2 had the same adsorption site as Co_1, i.e., Co_2-a (Fig. 2b), with an adsorption energy of -10.55 eV, and it formed bonds with four neighboring O atoms with bond lengths of 3 × 1.71 Å and 1.72 Å (Table 1). Comparison of the Co-Co bond lengths in the gas-phase structure reveals that Co-Co increased significantly after Co_2 adsorption (2.13 vs. 2.27 Å). The adsorption energy of Co_2 is 3.42 eV larger than Co_1, and the Co-O bond length was shortened by about 0.14 Å, which was attributed to the enhanced interaction between Co atoms and surface oxygen after the adsorption of Co_2. Here, we considered the initial adsorption geometry of Co_2 with the second Co atom sitting directly on top of the first Co atom without bonding to any surface atom (Fig. S3 Co_2-c), but after structural optimization, we found that Co_2 prefers to grow along the plane of $CeO_2(110)$ (Fig. 2b). It is worth mentioning that some of the models appeared large surface deformations after relaxation of the $Co_2/CeO_2(110)$ surface, which is attributed to the reactivity of the O ions on the $CeO_2(110)$ surface. For $CeO_2(110)$, oxygen vacancy formation energy is calculated to be 1.69 eV, which is much lower than 2.57 eV for $CeO_2(111)$ (Riley et al. 2018).

In the initial adsorption structure of Co_3, we considered the initial adsorption sites of ten Co_3 triangle structures

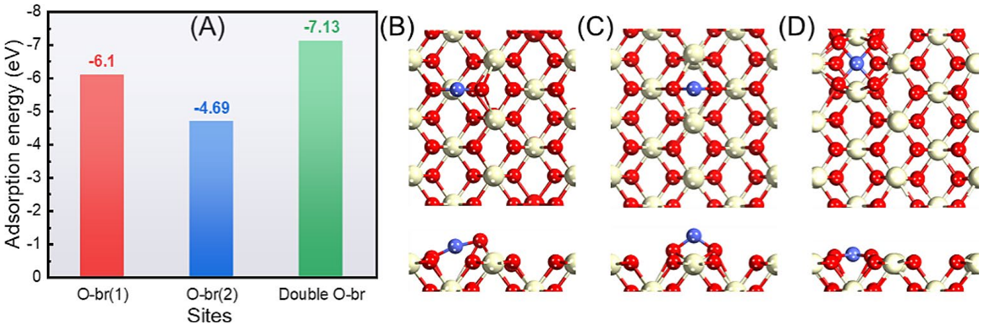

Fig. 1 Adsorption energies **a** of Co single atoms on the $CeO_2(110)$ surface and the top and front views of the corresponding stabilized adsorption configurations (O-br (1) **b** O-br (2) **c** and Double O-br **d**)

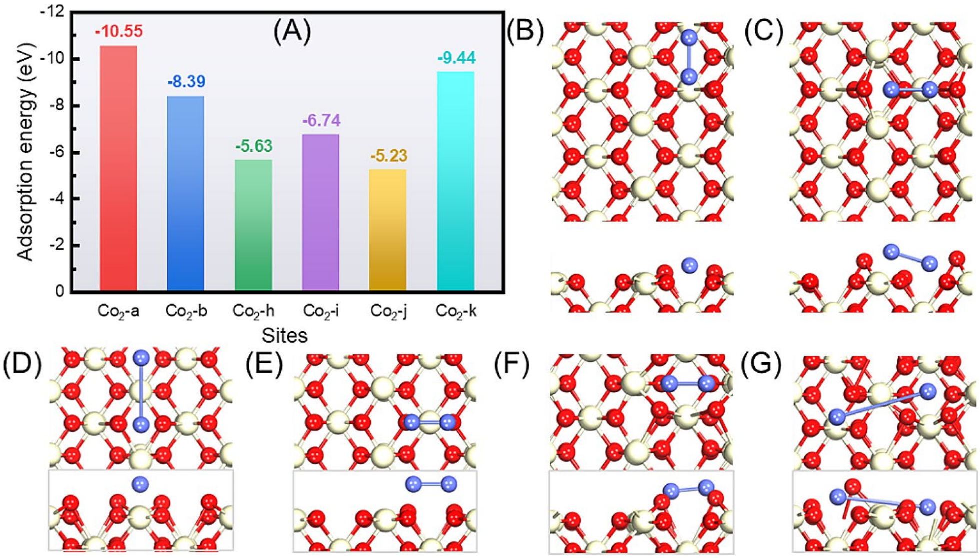

Fig. 2 Adsorption energies **a** of Co_2 cluster on the $CeO_2(110)$ surface and the top and front views of the corresponding stabilized adsorption configurations. **b-g** Correspond to the models of Co_2-a, b, h, i, j, k, respectively

Table 1 The geometric, energy and electronic properties of the surface of $CeO_2(110)$ adsorbed by Co_x were calculated

Models	$\bar{d}_{Ce-O}$(Å)	$\bar{d}_{Co-Co}$(Å)	d_{Co-O}(Å)	d_{Co-Ce}(Å)	$E^{ads}_{Co_x}$(eV)	Q_{Co}(|e|)
$Co_1/CeO_2(110)$	2.20, 2.68	-	3 × 1.85, 1.84	2 × 2.96	-7.13	-0.44
Co_2-a/$CeO_2(110)$	2.40, 2.98	2.27	3 × 1.71, 1.72	3.29, 3.28	-10.55	-0.24
Co_3-d/$CeO_2(110)$	2.55, 3.00	2.34	1.74, 1.78, 1.69, 1.75, 1.77	3.10, 3.12, 2.83	-12.31	-0.20
Co_{4-t}-b/$CeO_2(110)$	2.53, 2.74	2.30	1.73, 1.82, 1.77, 2 × 1.75	3.26, 3.11, 2.78	-11.87	-0.25
Co_{4-p}-i/$CeO_2(110)$	3.11	2.32	1.73, 1.78, 2.04, 1.93, 1.79, 1.67	2.65, 3.06, 2.98	-9.82	-0.23
Co_5-c/$CeO_2(110)$	2.49, 3.15	2.32	2 × 1.79, 2 × 1.83, 2 × 1.72	2 × 3.89, 3.39, 2.91	-12.65	-0.29
Co_6-f/$CeO_2(110)$	2.61, 3.35	2.33	4 × 1.78, 2 × 1.74	3.34, 2.77	-11.49	-0.23

$\bar{d}_{Ce-O}$ corresponds to the average Ce^{3+}-O (or Ce^{4+}-O) bond length near the Co_x adsorption site. The distances of undistorted surface Ce and surface O, as well as surface O and subsurface Ce, are 2.32 and 2.35 Å, respectively. $\bar{d}_{Co-Co}$(Å) is the average Co-Co bond length. d_{Co-O}(Å) and d_{Co-Ce}(Å) are the distances between the adsorbed Co_x and the adjacent O and Ce atoms. $E^{ads}_{Co_x}$ is the adsorption energy of Co_x ($x = 1 \sim 6$) cluster on the support $CeO_2(110)$ surface. Q_{Co} is the average charge gain/loss per Co atom of Co atoms in contact with the surface. The integers for d_{Co-O}(Å) and d_{Co-Ce}(Å) denote the number of Co-O and Co-Ce at the same distance, respectively

and explored the two most likely adsorption sites of Co_3 linear structure (Fig.S4), six stable adsorption models were obtained after structural optimization (Fig. 3). The initial adsorption models of Co_3-(b, c, g, i) and Co_3-(d, j, k, l) formed two final adsorption configurations, Co_3-b (Fig. 3c) and Co_3-d (Fig. 3d), respectively, after surface relaxation, while Co_3-a, e, f, h (Figs. 3b, e-g) formed independent adsorption configurations. The third Co atom in the initially adsorbed Co_3-b (Fig. 3c) and Co_3-h (Fig. 3g) grew along near and distant $CeO_2(110)$ surfaces, respectively, which was found to be preferred by the third Co atom to grow along away from the $CeO_2(110)$ surface after surface relaxation. Two typical linear $Co_3/CeO_2(110)$ models exhibited the largest adsorption energies after structural relaxation, -14.98 (Fig. 3e) and -13.43 eV (Fig. 3f), respectively. However, the optimized Co_3 was no longer a cluster structure, with Co-Co interstitial distances of 2.81 and 3.51 Å, respectively, hence they were not applicable to the discussion with the present work. The adsorption model of Co_3-d (Fig. 3d) was confirmed to be the most stable in the present work as it had the largest adsorption energy other than Co_3-e and Co_3-f with −12.31 eV. In the Co_{3-d} model, two cobalt atoms were stably deposited on the Double-O bridge site, while a third cobalt atom was laterally adsorbed along the O-br (2) site, forming five Co-O bonds averaging 1.75 Å in length (Table 1). By the action of the third Co atom, one O ion on the surface of $CeO_2(110)$ protrudes from the surface (2.55/3.00 Å), which was attributed to the asymmetry of the interaction of the third Co atom with the surface O (Nolan 2012). When the cobalt ion undergoes electron transfer with the surface oxygen, the symmetry of the structure is broken, causing a Ce ion to be reduced, increasing the Ce-O distance of that particular cerium atom (Nolan 2012). This phenomenon was similar to the previously reported overflow of O from the CeO_2 surface, and this metal-oxide interaction explained the extraordinary structure-activity dependence of cerium oxide-based catalysts (Song and Hensen 2013; Vayssilov et al. 2011).

According to previous studies, the Co_4 cluster had two stable configurations, the most stable planar rhombic

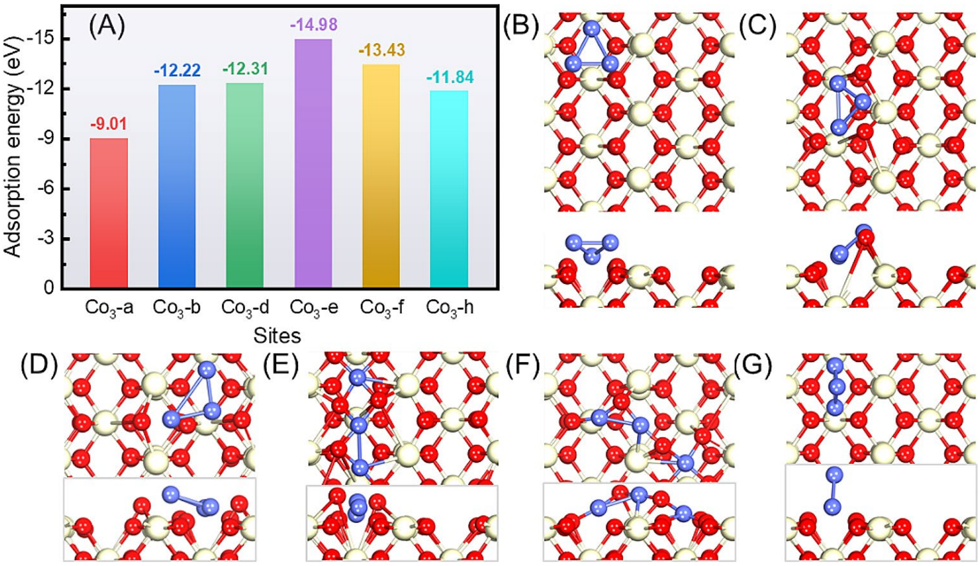

Fig. 3 Adsorption energies **a** of Co_3 cluster on the $CeO_2(110)$ surface and the top and front views of the corresponding stabilized adsorption configurations. **b**-**g** Correspond to the models of Co_3-a, b, d, e, f, h respectively

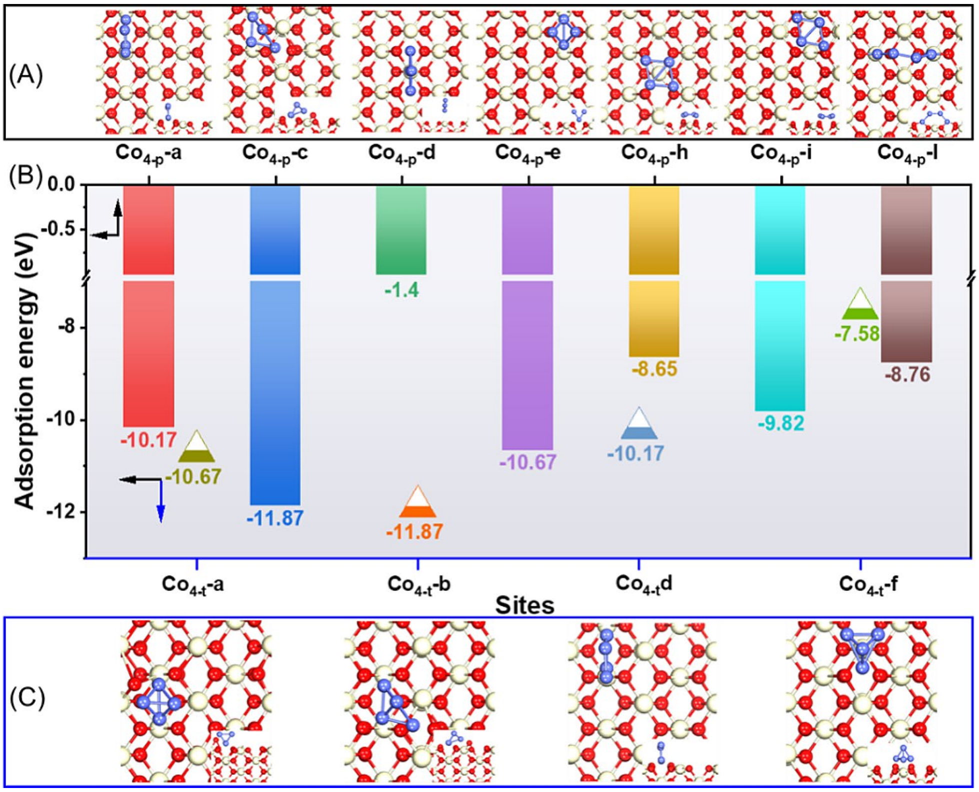

Fig. 4 **a** Stable adsorption configuration (top view and front view) of $Co_{4-p}/CeO_2(110)$ models. **b** Adsorption energy comparison of stable adsorption of Co_4 clusters. **c** Stable adsorption configuration (top view and front view) of $Co_{4-t}/CeO_2(110)$ models

structure (Co_{4-p}), and the sub-stable space tetrahedron structure (Co_{4-t}, Fig. S1) (Datta et al. 2007; Ma et al. 2006). In this work, we considered 22 and 9 initial adsorption sites of Co_{4-p} and Co_{4-t}, respectively, as shown in Fig. S5 and Fig. S6. After systematic optimization of different initial configurations and considering the symmetry breaking, seven and four stable adsorption configurations were obtained, respectively, as shown in Figs. 4a and c. Their corresponding adsorption energies were shown in Fig. 4b. For Co_{4-p}, the initially adsorbed Co_{4-p}-(a, b, k), Co_{4-p}-(c, f, o, q), Co_{4-p}-(e, g, j, p, r, t, u, v) and Co_{4-p}-(l, m, n, s) models were structurally optimized to four stable adsorption configurations, i.e., Co_{4-p}-a, Co_{4-p}-c, Co_{4-p}-e and Co_{4-p}-l (Fig. 4a). While the remaining Co_4-p adsorption models were all optimized to form independent configurations, see Fig. 4a. For Co_{4-t}, the initially adsorbed Co_{4-t}-(a, c) and Co_{4-t}-(b, j, h, i) sites were structurally optimized for the Co_{4-t}-a and Co_{4-t}-b models (Fig. 4c), respectively. The Co_{4-p}-d and Co_{4-p}-f adsorption models formed separate stable adsorption structures after surface relaxation,

Table 2 E_B, E_{Co-Co} and $E_{Co-O(Ce)}$ are the binding energy per atom, Co-Co cohesion energy and Co-substrate adhesion energy of Co clusters from planar to space structural configurations

	E_B (eV/per Co)	E_{Co-Co} (eV)	$E_{Co-O(Ce)}$ (eV)
$Co_2/CeO_2(110)$	-5.82	1.20	-7.03
$Co_3/CeO_2(110)$	-4.96	1.51	-6.47
Co_{4-p}-i/ $CeO_2(110)$	-3.70	-1.84	-1.86
Co_{4-t}-b/ $CeO_2(110)$	-4.50	-2.57	-1.93

respectively, see Fig. 4c. Interestingly, both the planar and space structures of Co_4 cluster adsorption eventually form the identical most stable adsorption configurations (Co_{4-p}-c in Fig. 4a and Co_{4-t}-b in Fig. 4c) with adsorption energy of -11.87 eV.

The ability of Co atoms to grow on the $CeO_2(110)$ surface to form a three-dimensional (3D) cluster structure may depend on the delicate balance between atom-atom interactions and atom-surface interactions (Mao et al. 2016). Therefore, to evaluate the stability of the $Co_x/CeO_2(110)$ system and the growth pattern of Co on the $CeO_2(110)$ surface, Table 2 calculated and summarized the E_B, E_{Co-Co} and $E_{Co-O(Ce)}$ for the transition of Co clusters from planar to 3D structural configurations. Here, the two-dimensional adsorption structures of Co_x, i.e., Co_2, Co_3 and Co_{4-p}, all of them had a larger $E_{Co-O(Ce)}$ than E_{Co-Co}, which implied that the interaction of Co with the $CeO_2(110)$ surface was stronger than the Co-Co interaction. In other words, the two-dimensional adsorption structure at this point was difficult to grow Co longitudinally along the surface due to the strong Co-O(Ce) bonding. Co_{4-t} was the smallest 3D structure of cobalt, and although all four Co atoms of Co_{4-p} interacted with surface oxygen, the E_B of $Co_{4-t}/CeO_2(110)$ was 0.8 eV larger than that of $Co_{4-p}/CeO_2(110)$, which may be due to the strong Co-Co interaction in $Co_{4-t}/CeO_2(110)$, implying that the Co_{4-t} interaction with $CeO_2(110)$ surface is stronger. The difference in E_{Co-Co} between $Co_{4-t}/CeO_2(110)$ and $Co_{4-p}/CeO_2(110)$ was very close to 0.8 eV, while $E_{Co-O(Ce)}$ was almost equal. When Co_{4-t} was loaded on $CeO_2(110)$, the E_B was mainly contributed by E_{Co-Co}, and the Co-Co interaction was strong and the charge transfer was significant (0.25 vs. 0.23 e/per Co atom, Table 1). Additionally, E_{Co-Co} rapidly increased and approached more closely the metal cohesion energy of bulk phase Co (4.40 eV) (Singal and Das 1977) when the number of deposited Co atoms reached the conditions for the formation of 3D structures, implying that as Co-O(Ce) interactions weaken, Co-Co interatomic interactions increase ($E_{Co-Co} > E_{Co-O(Ce)}$) and clusters above Co_4 cluster structure preferentially forms a 3D stereo structure.

Based on the above findings, we loaded simple 3D structure of Co_5 and Co_6 clusters on the surface of $CeO_2(110)$ to determine an optimal $Co_x/CeO_2(110)$ structure for studying the methane activation mechanism. Fifteen initial Co_5 adsorption configurations (Fig. S7) were structurally optimized to form ten stable adsorption models (Fig. 5). Specifically, the initial adsorption Co_5-(b, e), Co_5-(c, g, k), Co_5-(j, l) and Co_5-(m, o) sites correspond to the optimized models Co_5-b, Co_5-c, Co_5- j and Co_5-m in Fig. 5(c, d, i, j), respectively. While the remaining Co_5 adsorption models were all

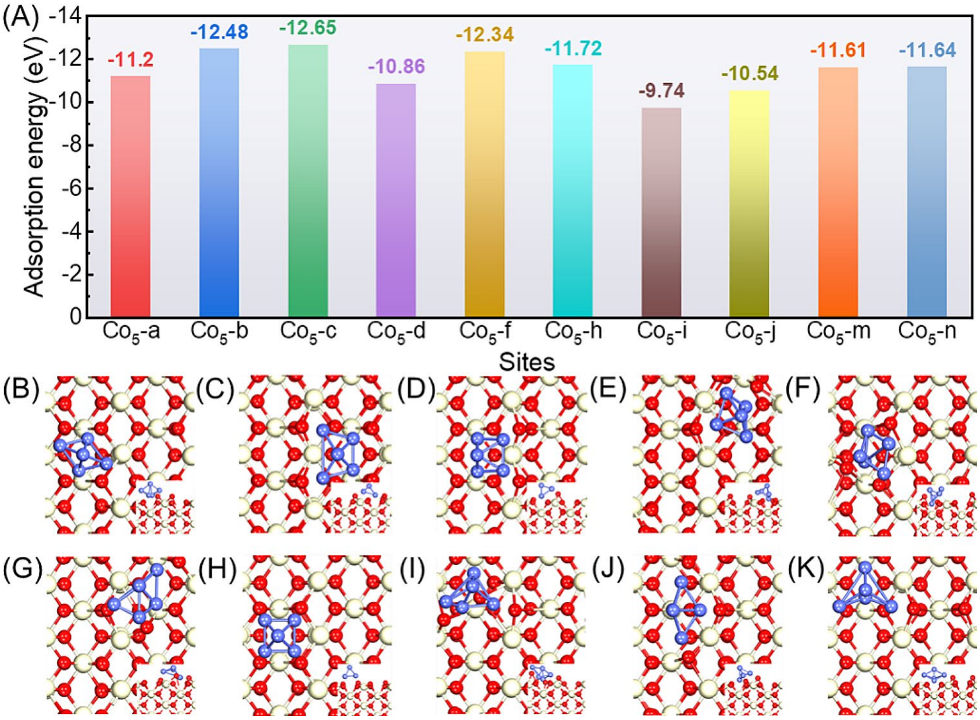

Fig. 5 Adsorption energies **a** of Co_5 cluster on the $CeO_2(110)$ surface and the top and front views of the corresponding stabilized adsorption configurations. **b-k** Correspond to the models of Co_5-a ~ d, f, h, i, j, m, n respectively

optimized to form independent structures, see Fig. 5(b, e, f, g, h, k). Comparison of the initial adsorption model and the final results reveals that the Co atoms in the initial adsorption structure interact strongly with the O atoms on the surface of $CeO_2(110)$. Specifically, Co clusters would migrate from unstable positions to stable adsorption sites, with surface O ions detaching from the surface in the effect of Co, destroying the original structural symmetry. Comparison of the stable adsorption models revealed that Co_5-c (Fig. 5d) had the largest adsorption energy of -12.65 eV and was considered to be the most stable adsorption configuration. The four Co atoms of the bottom layer interact with six O atoms on the surface of $CeO_2(110)$ with an average Co-O bond length of about 1.79 Å. Similar to Co_2, Co_3 and Co_4, two of the four Co atoms in the bottom layer remain in the double oxygen bridge site, while the other two Co atoms interact with the two O atoms in the lateral double oxygen bridge site and make them bulge on the surface. Furthermore, the Mulliken charge distribution analysis in Table 1 shows that the Co_5-c/$CeO_2(110)$ model has the largest charge transfer (0.29 e/per Co atom) after adsorption of all Co clusters, which implies that Co has the strongest interaction with the substrate $CeO_2(110)$ in this structure.

In this work, nine initial adsorption models of Co_6 on $CeO_2(110)$ were considered (as shown in Fig. S8), and no identical stable adsorption model was found after surface relaxation (as shown in Fig. 6). Co_6-c/$CeO_2(110)$ (Fig. 6d) exhibited the largest adsorption energy of all the Co_6 adsorbates, yet it was not the most stable structure we need for reasons consistent with the previously discussed unsuitability of Co_2-k (Fig. 2g), Co_3-e (Fig. 3e) and Co_3-f (Fig. 3f). Specifically, one of the Co atoms in the Co_6-f/$CeO_2(110)$ structure had detached from the Co cluster and interacts with the surface alone, and its distanced from the closest O are approximately 1.81 Å, with distanced to the closest Co of 2.44 and 2.58 Å (d_{Co-Co} = 2.30 Å in the Co_6 cluster, Fig. S1). Therefore, Co_6-f/$CeO_2(110)$ was considered to be the most stable adsorption model for the adsorption of Co_6 clusters on $CeO_2(110)$ with an adsorption energy of -11.49 eV. The stable adsorption sites of the Co_6 cluster were similar to those of the other Co clusters, all belonging to the $CeO_2(110)$ surface depression with the presence of more O ions. only four Co atoms in the Co_6-f/$CeO_2(110$ configuration were bonded to surface O, which implied that the surface interaction of the Co_6 cluster with $CeO_2(110)$ is weaker than that of the Co_5 cluster. This was also supported by Mulliken charge distribution analysis (0.29 vs. 0.23 e/per Co atom). Moreover, the average bond length of the five Co atoms of Co_6 to the surface O ions was essentially the same as that in Co_5 (1.80 vs. 1.77 Å). It was noteworthy that Co_6 adsorption on $CeO_2(110)$ was weaker than the most stable Co_5 adsorption on $CeO_2(110)$ in all possible structures we considered, implying that the structural stability of Co clusters decreased as the number of Co atoms in $Co_x/CeO_2(110)$ increased to 6. The Co_6-c/$CeO_2(110)$ model with the largest adsorption energy accompanied by the detachment of one Co atom also supports this.

From the above discussion, we could conclude that the stable adsorption site of single-atom Co on the $CeO_2(110)$ surface is the Double O-br site, Co prefers to form 3D clusters on the $CeO_2(110)$ surface, and the stability of the clusters decreases when the number of atoms in the adsorbed Co clusters is more than six. Furthermore, the stable Co_5-c/$CeO_2(110)$ structure has the largest adsorption energy, suitable Co-Co atomic interactions, and Co atom-$CeO_2(110)$ surface interactions, which should be regarded as the optimal $Co_x/CeO_2(110)$ structure for the study of methane activation mechanism.

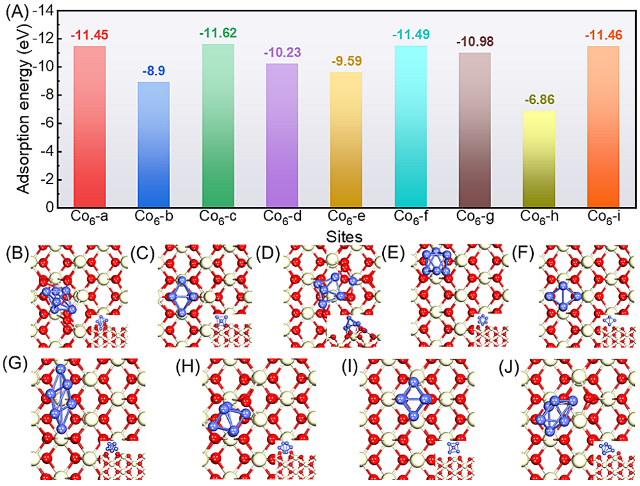

Fig. 6 Adsorption energies **a** of Co_6 cluster on the $CeO_2(110)$ surface and the top and front views of the corresponding stabilized adsorption configurations. **b-j** Correspond to the models of Co_6-a ~ i respectively

3.2 Electronic structures of Co_x ($x = 1 \sim 6$) on $CeO_2(110)$ surface

It is well known that density of states (DOS) is a very helpful tool for electronic structure analysis in flat plate model calculations. Here, we have analyzed the partial density of states (PDOS) for the most energetically favorable $Co_x/CeO_2(110)$ structure and further elucidated the Co_x and $CeO_2(110)$ interactions by electronic structure properties. The PDOS of the stabilized $Co_x/CeO_2(110)$ structure was illustrated in Fig. 7. The dashed and solid lines in the PDOS describing Co_x indicated the electronic states of Co in the gas phase and adsorbed on the surface of $CeO_2(110)$, respectively. The dashed and solid lines in the PDOS of $CeO_2(110)$ described the electronic states of O and Ce, respectively. The contributions of the basal Ce and O atoms to TDOS after adsorption of Co atoms or clusters were essentially unchanged significantly (not shown in the paper). However, a shift in their electron-occupying states toward lower energies can be clearly observed, which is consistent with the results for other transition metals after adsorption (Chutia et al. 2018; Qin and Su 2021; Tian et al. 2018). In contrast to the pure $CeO_2(110)$ surface PDOS, new occupied states appeared between the top of the valence band and the bottom of the Ce-4f band. This occupied state is almost entirely contributed by the 4f orbital of the reduced Ce^{3+} ion, the 3d orbital of the Co^{n+} ion, and the 2p orbital of the O^{2-} ion (Li et al. 2016). This is in agreement with the work reported by Zhang et al. (2021) studying the surface of Co-doped $CeO_2(110)$.

When Co_x was adsorbed to the surface, the occupied 4s state of Co_x near the Fermi energy level disappeared almost completely, implying that the transfer of Co-4s electrons occurs upon adsorption (Cui et al. 2012). The Co-3d states can be observed to spread over a wider energy range above the Fermi level, indicating strong interactions between Co_x and on the support surface with greater charge transferred between Co and O atoms (Reddy and Deshpande, 2022). The asymmetry of the Co-3d spin states was observed in the PDOS, suggesting the presence of a non-zero magnetic moment on the Co atom. Co loading resulted in the formation of occupied d-type Co orbitals in the bandgap of the semiconducting properties of the $CeO_2(110)$ surface, which was consistent with the f-type orbitals that were previously found to be occupied upon Ni loading (Hahn et al. 2015). The PDOS area and height of Co orbitals increased with the number of Co atoms, indicating that the electron density increased with the number of Co atoms (Xu et al. 2016). The increase in the electronic occupation state of Co-3d orbitals resulted in a decrease in the band gap, which completely disappeared from Co_3 onwards (Fig. 7c). Similar to the results of Pintos et al. (2013), we found new unoccupied states above the Fermi energy level of the PDOS curve, mainly contributed by O-2p orbitals and Co-3d orbitals. The crossover between O-2p and Co-3d orbitals indicated that some O atoms in $CeO_2(110)$ were activated by some Co atoms in the Co cluster, leading to the formation of Co-O bonds. As depicted by PDOS in Fig. 7e, the contribution of O-2p orbitals in the interstitial state (-2 to -0.8 eV) after the adsorption of Co_5 largely overlapped with that of Co_3-d orbitals, whereas the contribution from the O-2p orbitals after the adsorption of all Co_x except Co_1 were smaller than those from the Co-3d orbitals. The stronger interaction between O and Co atoms in the $Co_5/CeO_2(110)$ structure was explained, which was consistent with the result that Co_5 exhibited the maximum adsorption energy after adsorption. It is remarkable that the contribution of O-2p orbitals in the interstitial state (-2 to -1.5 eV) after Co_1 adsorption was larger than that of Co-3d orbitals, which was due to the interaction of Co_1 with the four O atoms on the surface after stable adsorption, and the transfer of electrons from surface Ce ions to Co via O. In addition, the asymmetric behavior of the electron-occupying states of Co near the Fermi energy level indicated the metallic character of the $Co_x/CeO_2(110)$ system (Hahn et al. 2015; Xu et al. 2016).

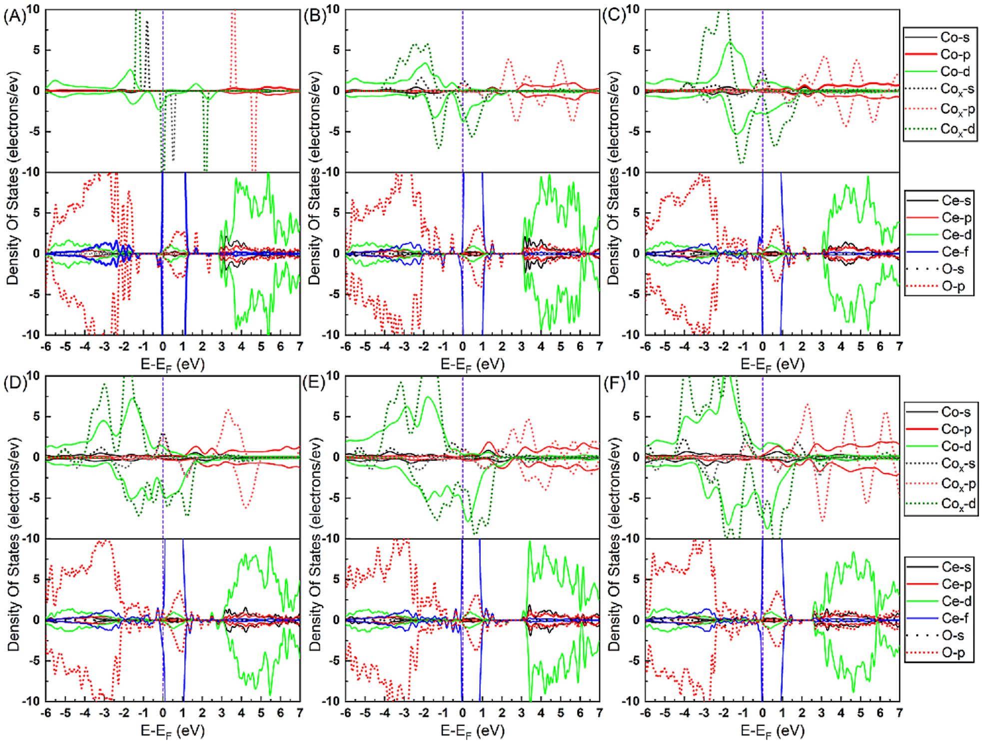

Fig. 7 Projected density of states (PDOS) on the atoms involved for **a** $Co_1/CeO_2(110)$, **b** $Co_2/CeO_2(110)$, **c** $Co_3/CeO_2(110)$, **d** $Co_4/CeO_2(110)$, **e** $Co_5/CeO_2(110)$ and **f** $Co_6/CeO_2(110)$ surface. E_F is the Fermi energy level and is taken as the zero point of DOS. Upper and lower panels represent spin up and spin down, respectively

According to Mulliken charge analysis (Table 1), the strong interaction of the Co clusters with the $CeO_2(110)$ surface led to a significant charge transfer from the metal atoms as well as a partial oxidation of Co atoms close to the surface of the supported $CeO_2(110)$ (Li et al. 2019), with Q_{Co} ranging from 0.20 to 0.44 e/per Co atom. The charge transfer on each Co atom was 0.29 and 0.23 e for the CeO_2-supported Co_5 and Co_6 systems, respectively, i.e., the $Co_5/CeO_2(110)$ configuration had more electron transfer, which could lead to stronger interactions (Qu and Wang 2022). Noteworthy, although the maximum charge transfer after single-atom Co adsorption would have implied a stronger cobalt-support interaction, the disappearance of the highly localized d-orbital contribution in PDOS after single-atom Co adsorption implied that the low-activity d-orbital electrons might have reduced the redox capacity of the catalyst (Shi et al. 2021). Moreover, the average distance between Ce and the nearest neighboring O ion near the adsorption site of the Co_5 cluster was calculated to be 2.49 Å, which is similar to the experimentally found Ce^{3+}-O bond length (2.50 Å) (Ganduglia-Pirovano et al. 2009). The optimized $Co_5/CeO_2(110)$ structure was selected as the optimal configuration for the study of methane activation mechanism by considering the adsorption energy, binding energy and Co atom- $CeO_2(110)$ surface electron interactions comprehensively.

3.3 Adsorption of $CH_x (x = 0 \sim 4)$ over $Co_5/CeO_2(110)$

Stable adsorption sites for CH_x* species were identified via the most stable CH_4 adsorption sites, which can overcome the high energy barrier to long-range migration of CH_x* species during CH_4 dissociation (Singha et al. 2019). The $Ni_5/CeO_2(110)$ model identified for the study of methane activation has three possible CH_4 molecular adsorption sites: (i) surface adsorption site, (ii) interfacial adsorption site, (iii) active metal Co adsorption site (see Fig. S9). There are five stable structures of CH_4 after adsorption at the surface adsorption site (Fig. S10) with adsorption energies ranging from -0.07 to -0.19 eV, while there is only one stable structure at both the interfacial adsorption site and the metal site. The stable structure of CH_4 after adsorption at the interfacial adsorption site with an adsorption energy of -0.12 eV is shown in Fig. S10. The CH_4 adsorbed on the top of Co_5 had the largest adsorption energy of -0.45 eV, which was considered to be the most stable adsorption model for methane, as shown in Fig. 8a. The C-H_1, C-H_2, C-H_3 and C-H_4 bond lengths after CH_4 adsorption are 1.14, 1.13, 1.10 and 1.10 Å, respectively; the H-C-H angles are 104.83-114.65° (the C-H bond length of methane molecule in the gas phase is 1.10 Å and the H-C-H angle is 109.47° (Horn and Schlögl 2015). It implied that the CH_4 molecule was effectively activated during the adsorption process (Guo and Wang 2017).

The most stable adsorption structures and adsorption energies of CH_x* and H* at the Co metal sites are shown in Figs. 8b-f, respectively, which could be used to determine the final structures of the methane dissociation products. In addition, other adsorption configurations of CH_x* species and H* species after methane dissociation are also shown in the Supplementary material.

3.4 Energetics of dissociation CH_4

To understand the activation mechanism of CH_4 on the surface of $Co_5/CeO_2(110)$ catalyst, the activation energy (E_a) and reaction energy (E_{re}) for the sequential dehydrogenation of methane at the above adsorption sites have been investigated. The energy information of the stepwise dehydrogenation process of methane and the structural information of the transition state were summarized in Table 3. Methane adsorbed on the top of Co_5 was used as the initial state (IS), and the first efficiently activated C-H bond (C-H_1) dissociated on the metal to form the transition state (TS, see Fig. 9a) with a C–H distance of 1.67 Å. Here, the H atom of the dissociated first C-H bond is extracted by the active Co metal and combined with the bridge of the Co-Co bond to form two Co-H bonds, while the CH_3* fragment adsorbs to the Co metal on the other side to form two Co-C bonds. The transition state search revealed that the E_a to be overcome by methane to dissociate the first C-H bond at the active metal site of Co_5-$CeO_2(110)$ was only 0.44 eV(about 10.10 Kcal/mol), which is much lower than the E_a (23.70 Kcal/mol) of CH_4 dissociation catalyzed by Ni_4 cluster supported on cerium oxide reported by Singha et al. (2019), and is close to the E_a of 0.55 eV reported by Lustemberg et al. (2020) for the dissociation of CH_4 on the Co_4/Ce_2O_3. Moreover, the E_{re} for the dissociation of the first C-H bond was -0.41 eV, implying that the process is thermodynamically favorable.

The energy and structure diagrams for the continued dehydrogenation of CH_3* to form CH_2*+H* were shown in Fig. 9b. The E_a for the continued dehydrogenation of CH_3* was 0.55 eV, which is higher than that for the first C-H bond dissociation of CH_4, implying that that the rate-determining step (RDS) for methane activation in the $Co_5/CeO_2(110)$ catalyst system studied in this paper was no longer the activation of the first C-H of CH_4 as previously widely reported (Egawa 2018; Wei and Iglesia 2004). One surprising result was that the continued dehydrogenation of CH_3* was an exothermic reaction with a E_{re} of -0.11 eV, which was contrary to the results of previous studies on Ni (Xie et al. 2021) and Pt (Niu et al. 2016) as reactive metals. The activated C-H bond was extended from 1.12 Å to 1.66 Å in the TS where CH_3* continued to dissociate and dehydrogenate, and the distances between the dissociated H atom and Co are

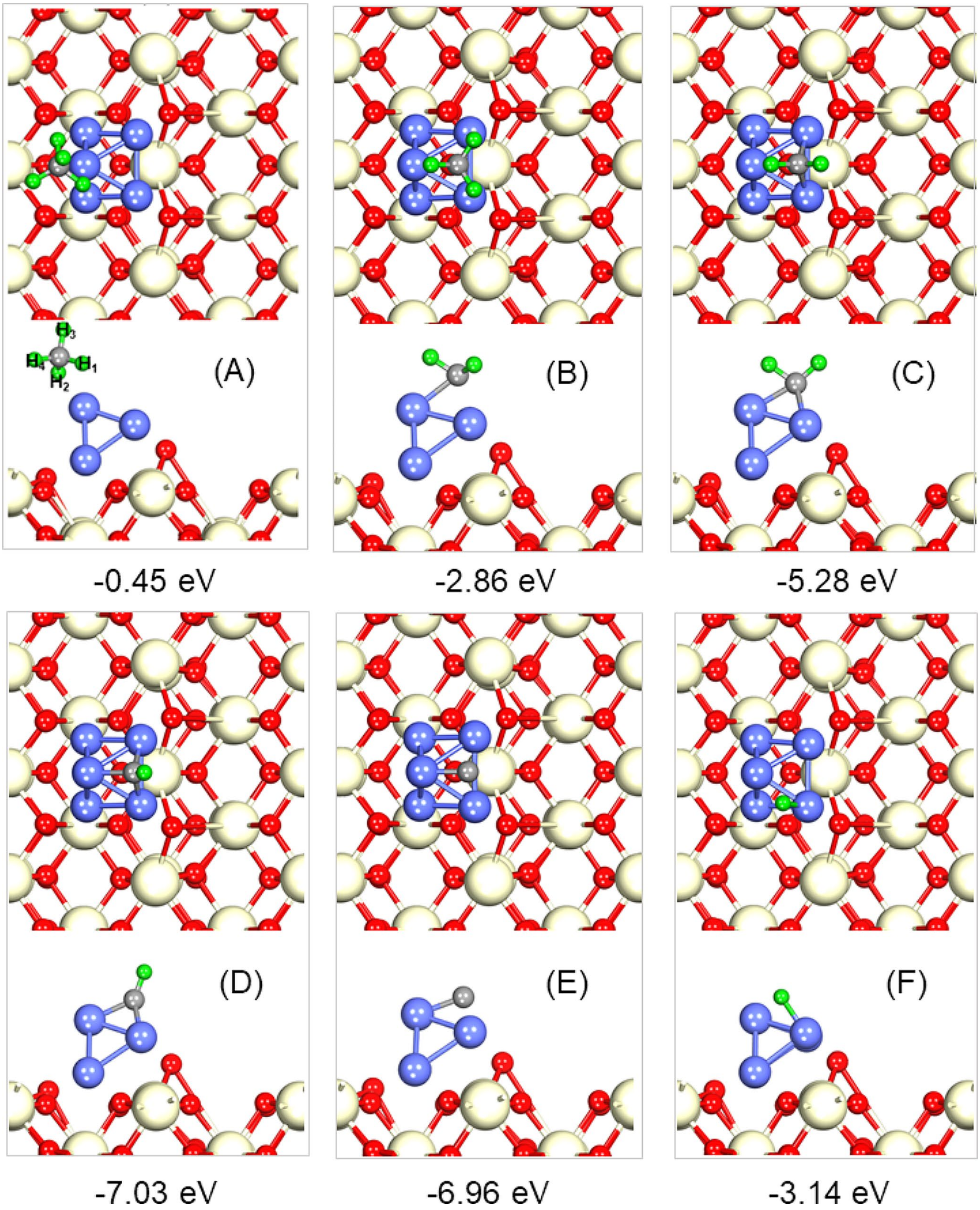

Fig. 8 Stable adsorption sites and adsorption energies of **a** CH_4* **b** CH_3* **c** CH_2* **d** CH* **e** C* and **f** H* species on the surface of $Co_5/CeO_2(110)$ catalyst. Includes top view (top) and front view (bottom)

Table 3 The activation energies (E_a) and reaction energies (E_{re}) during the stepwise dissociation reaction of methane, as well as the distance between each dissociated transition state C and H

Step	E_a (eV)	E_{re} (eV)	d_{C-H} (Å)
CH_4*→CH_3*+H*	0.44	-0.41	1.67
CH_3*→CH_2*+H*	0.55	-0.11	1.66
CH_2*→CH*+H*	0.31	-0.11	2.26
CH*→C*+H*	1.20	0.54	1.57

2.13 Å and 1.51 Å, respectively, implying that the H atom forms a strong bond with Co (Li et al. 2014).

The dissociation process of CH_2* was shown in Fig. 9c, in which the hydrogen atom directed towered the top Co atom was stretched to its top and directed towered the hcp site of the three Co atoms in the rear side, and eventually the hydrogen atom was firmly bonded to the three Co atoms in the rear hcp sites. While the hydrogen atoms on CH* fragment moved to the top of C atom, and the whole CH* fragment was still adsorbed at the hcp site on the upper part of Co_5 cluster. DFT calculations of the transition state structure revealed that the C-H bond was pulled from 1.10 Å to 2.26 Å, and the CH_2* dehydrogenation to CH* required to overcome an E_a of 0.31 eV (about 7.13 kcal/mol), the E_{re} is -0.11 eV. This E_a is greater than the recently reported Pt(111) surface CH_2* dehydrogenation barrier(6.20 kcal/mol) (Yoshida et al. 2022), which is very consistent with the Ni(111) surface CH_2* dehydrogenation barrier(0.30 eV) reported by Blaylock et al. (2009).

The E_a for CH* dehydrogenation is 1.20 eV (see Fig. 9d), which agreed well with Li et al. (2014) (1.36 eV). The transition state configuration showed that the hydrogen atom was pulled from the top of the C atom to the Co-Co bridge site, and the C-H bond was pulled from 1.10 Å to 1.57 Å.

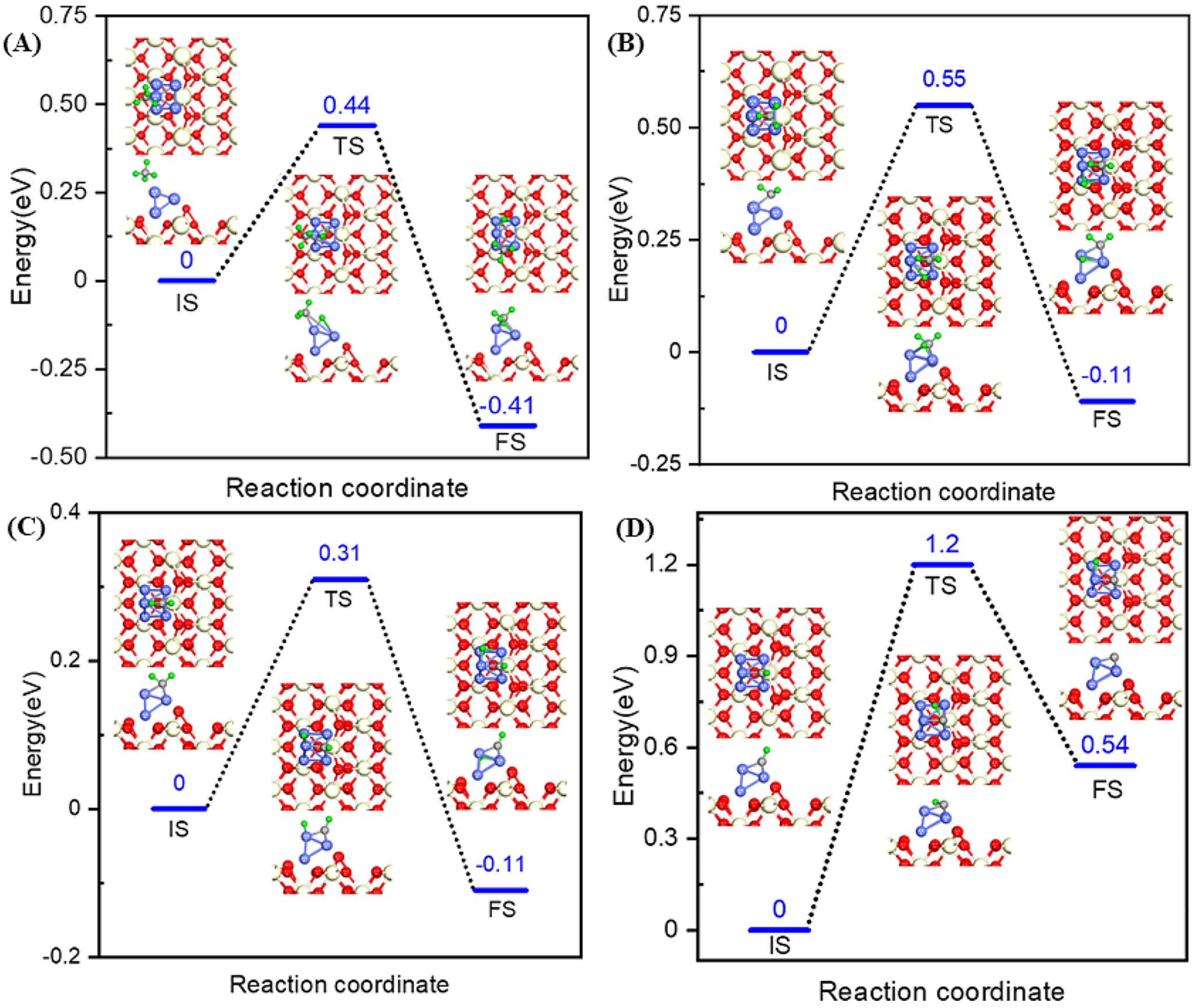

Fig. 9 Energy diagrams for complete dissociation of methane. The initial, transition and final states of the reaction for each dehydrogenation step were inserted separately into the blanks of each energy diagrams

In the configuration of the product, C and H atoms were located at two hcp sites, respectively, which was the same as CH* dehydrogenation. In addition, CH* dehydrogenation was calculated to be an endothermic reaction with a E_{re} of 0.54 eV. The dehydrogenation of CH* was the RDS in this research system, which was consistent with the previous reports on the difficulty of further dissociation of carbon deposits after methane activation (Niu et al. 2016; Xie et al. 2021).

4 Conclusions

In this work, we investigated the growth mode of small-sized Co clusters on the surface of $CeO_2(110)$ using density-functional theory and determined the most favorable Co cluster structure to be formed on $CeO_2(110)$. Co clusters grew most favorably at the step positions enriched with oxygen ions which are near the double-oxygen bridge sites. Single-atom Co, Co_2 clusters and two Co atoms in Co_3 clusters were all stable adsorbed at double-oxygen bridge sites on the surface of $CeO_2(110)$, while the third Co atom in Co_3 clusters grew along the side and adsorbed at the O bridge sites. The fourth Co atom in the Co_4 cluster grew along the direction away from the surface of $CeO_2(110)$ and formed a three-dimensional cluster, suggesting that Co clusters on $CeO_2(110)$ were more inclined to form three-dimensional rather than planar clusters. The Co_5 clusters formed on $CeO_2(110)$ were the most competitive among all the small-sized Co clusters considered. The primary reasons were that Co_6 cluster formation on $CeO_2(110)$ was thermodynamically limited compared to Co_5 clusters, as well as the Co atoms in Co_6 clusters had the ability to grow independently from the clusters with the structure being thermodynamically more favorable than other Co_6 clusters. The adsorption and activation mechanism of methane was investigated using the optimal $Co_5/CeO_2(110)$ model. The energetics of methane dissociation implied that the catalyst model had a methane activation capacity comparable to that of metallic nickel and platinum, with a dissociation energy barrier for the first C-H bond of only 0.44 eV. In addition, the high energy barrier for the dissociation of the CH* fragments provided an efficient route for selective methane activation.

Supplementary Information The online version contains supplementary material available at https://doi.org/10.1007/s40789-024-00697-7.

Acknowledgements This work was supported by the National Natural Science Foundation of China (52174279), the Analysis and Testing Foundation of Kunming University of Science and Technology (2022M20202202138), and Yunnan Fundamental Research Projects (202301AU070027).

Author contributions LH: Investigation, Methodology, Software, Formal analysis, Writing – original draft; DL: Data Curation; LJ: Visualization, Investigation; ZL: Formal analysis; DT: Conceptualization, resources, Writing – review and editing; KL: Funding acquisition, Project administration, Writing – review and editing.

Data availability The data that support the plots within this paper and other finding of this study are available from the corresponding author upon reasonable request.

Declarations

Conflict of interest There are no conflicts to declare.

References

Adachi G-y, Imanaka N (1998) The Binary Rare Earth Oxides. Chem Rev 98:1479–1514. https://doi.org/10.1021/cr940055h

Blankenship AN, Ravi M, Newton MA, van Bokhoven JA (2021) Heterogeneously Catalyzed Aerobic Oxidation of Methane to a Methyl Derivative. Angew Chem Int Ed 60:18138–18143. https://doi.org/10.1002/anie.202104153

Blaylock DW, Ogura T, Green WH, Beran GJO (2009) Computational investigation of Thermochemistry and kinetics of Steam methane reforming on Ni(111) under realistic conditions. J Phys Chem C 113:4898–4908. https://doi.org/10.1021/jp806527q

Chang W, Gao Y, He J, Xia X, Huang C, Hu Y, Xu W, Jiang B, Han Y, Zhu Y, Wang X (2023) Asymmetric coordination activated lattice oxygen in perovskite ferrites for selective anaerobic oxidation of methane. J Mater Chem A 11:4651–4660. https://doi.org/10.1039/D2TA09187A

Cheng Z, Zhang L, Jin N, Zhu Y, Chen L, Yang Q, Yan M, Ma X, Wang X (2021) Effect of calcination temperature on the performance of hexaaluminate supported CeO_2 for chemical looping dry reforming. Fuel Process. Technol. 218:106873. https://doi.org/10.1016/j.fuproc.2021.106873

Chutia A, Willock DJ, Catlow CRA (2018) The electronic properties of au clusters on $CeO_2(110)$ surface with and without O-defects. Faraday Discuss 208:123–145. https://doi.org/10.1039/c8fd00002f

Cui L, Tang Y, Zhang H, Hector LG, Ouyang C, Shi S, Li H, Chen L (2012) First-principles investigation of transition metal atom M (M = Cu, Ag, Au) adsorption on $CeO_2(110)$. PCCP 14:1923–1933. https://doi.org/10.1039/C2CP22720G

Datta S, Kabir M, Ganguly S, Sanyal B, Saha-Dasgupta T, Mookerjee A (2007) Structure, bonding, and magnetism of cobalt clusters from first-principles calculations. Phys Rev B 76:014429. https://doi.org/10.1103/PhysRevB.76.014429

Delley B (1990) An all-electron numerical method for solving the local density functional for polyatomic molecules. J Chem Phys 92:508–517. https://doi.org/10.1063/1.458452

Delley B (2000) From molecules to solids with the DMol^3 approach. J Chem Phys 113:7756–7764. https://doi.org/10.1063/1.1316015

Delley B (2006) Ground-State enthalpies: evaluation of electronic structure approaches with emphasis on the Density Functional Method. J Phys Chem A 110:13632–13639. https://doi.org/10.1021/jp0653611

Deng K, Lin L, Rui N, Vovchok D, Zhang F, Zhang S, Senanayake SD, Kim T, Rodriguez JA (2020) Studies of CO_2 hydrogenation over cobalt/ceria catalysts with in situ characterization: the effect of cobalt loading and metal-support interactions on the catalytic activity. Catal Sci Technol 10:6468–6482. https://doi.org/10.1039/D0CY00962H

Egawa C (2018) Methane dry reforming reaction on Ru(001) surfaces. J Catal 358:35–42. https://doi.org/10.1016/j.jcat.2017.11.010

Ganduglia-Pirovano MV, Da Silva JLF, Sauer J (2009) Density-functional calculations of the structure of Near-Surface Oxygen vacancies and Electron localization on CeO_2(111). Phys Rev Lett 102:026101. https://doi.org/10.1103/PhysRevLett.102.026101

García Pintos D, Juan A, Irigoyen B (2013) Mn-Doped CeO_2: DFT + U study of a Catalyst for oxidation reactions. J Phys Chem C 117:18063–18073. https://doi.org/10.1021/jp403911b

Guo D, Wang G-C (2017) Partial oxidation of methane on Anatase and Rutile defective TiO_2 supported Rh_4 cluster: a density functional theory study. J Phys Chem C 121:26308–26320. https://doi.org/10.1021/acs.jpcc.7b07489

Hahn KR, Seitsonen AP, Iannuzzi M, Hutter J (2015) Functionalization of CeO_2(111) by deposition of small ni clusters: effects on CO_2 adsorption and O vacancy formation. ChemCatChem 7:625–634. https://doi.org/10.1002/cctc.201402906

Halgren TA, Lipscomb WN (1977) The synchronous-transit method for determining reaction pathways and locating molecular transition states. Chem Phys Lett 49:225–232. https://doi.org/10.1016/0009-2614(77)80574-5

Horn R, Schlögl R (2015) Methane activation by heterogeneous catalysis. Catal Lett 145:23–39. https://doi.org/10.1007/s10562-014-1417-z

Huang L, Li D, Tian D, Jiang L, Li Z, Wang H, Li K (2022) Optimization of Ni-Based catalysts for dry reforming of methane via Alloy Design: a review. Energ Fuel 36:5102–5151. https://doi.org/10.1021/acs.energyfuels.2c00523

Kumari N, Sinha N, Haider MA, Basu S (2015) CO_2 reduction to methanol on CeO_2(110) surface: a density functional theory study. Electrochim Acta 177:21–29. https://doi.org/10.1016/j.electacta.2015.01.153

Li J, Croiset E, Ricardez–Sandoval L (2014) Effect of carbon on the Ni catalyzed methane cracking reaction: a DFT study. Appl Surf Sci 311:435–442. https://doi.org/10.1016/j.apsusc.2014.05.081

Li WQ, Goverapet Srinivasan S, Salahub DR, Heine T (2016) Ni on the CeO_2(110) and (100) surfaces: adsorption vs. substitution effects on the electronic and geometric structures and oxygen vacancies. PCCP 18:11139–11149. https://doi.org/10.1039/C6CP00738D

Li M-R, Song Y-Y, Wang G-C (2019) The Mechanism of Steam-Ethanol Reforming on Co_{13}/CeO_{2-x}: A DFT Study. ACS Catal 9:2355–2367. https://doi.org/10.1021/acscatal.8b03765

Li D, Xu R, Tian M, Jia Y, Gu Z, Zhu X, Li K (2020) Encapsulated $Co_3O_4/(SiAl@Al_2O_3)$ thermal storage functional catalysts for catalytic combustion of lean methane. Appl Therm Eng 181:116012. https://doi.org/10.1016/j.applthermaleng.2020.116012

Liu Z, Lustemberg P, Gutierrez RA, Carey JJ, Palomino RM, Vorokhta M, Grinter DC, Ramirez PJ, Matolin V, Nolan M, Ganduglia-Pirovano MV, Senanayake SD, Rodriguez JA (2017) In Situ Investigation of Methane Dry Reforming on Metal/Ceria(111) surfaces: metal-support interactions and C-H bond activation at low temperature. Angew Chem Int Ed 56:13041–13046. https://doi.org/10.1002/anie.201707538

Liu Z, Li J, Buettner M, Ranganathan RV, Uddi M, Wang R (2019) Metal-support interactions in CeO_2- and SiO_2-Supported cobalt catalysts: effect of support morphology, reducibility, and Interfacial Configuration. ACS Appl Mater Interfaces 11:17035–17049. https://doi.org/10.1021/acsami.9b02455

Lustemberg PG, Zhang F, Gutiérrez RA, Ramírez PJ, Senanayake SD, Rodriguez JA, Ganduglia-Pirovano MV (2020) Breaking simple scaling relations through metal–oxide interactions: understanding room-temperature activation of methane on M/CeO_2 (M = Pt, Ni, or Co) Interfaces. J Phys Chem Lett 11:9131–9137. https://doi.org/10.1021/acs.jpclett.0c02109

Ma Q-M, Xie Z, Wang J, Liu Y, Li Y-C (2006) Structures, stabilities and magnetic properties of small Co clusters. Phys Lett A 358:289–296. https://doi.org/10.1016/j.physleta.2006.05.033

Ma T, Liu J, Fu J, Wu B (2022) Drilling and completion technologies of coalbed methane exploitation: an overview. Int J Coal Sci Techn 9:68. https://doi.org/10.1007/s40789-022-00540-x

Mao J, Li S, Zhang Y, Chu X, Yang Z (2016) Density functional study on the mechanism for the highly active palladium monolayer supported on titanium carbide for the oxygen reduction reaction. J Chem Phys 144:204703. https://doi.org/10.1063/1.4952416

Martono E, Vohs JM (2012) Support effects in cobalt-based ethanol steam reforming catalysts: reaction of ethanol on Co/CeO_2/YSZ(100) model catalysts. J Catal 291:79–86. https://doi.org/10.1016/j.jcat.2012.04.010

Mastalerz M, Drobniak A (2020) 5-Coalbed methane: reserves, production, and Future Outlook. In: Letcher TM (ed) Future Energy, 3rd edn. Elsevier, Amsterdam, The Netherlands, pp 97–109. https://doi.org/10.1016/B978-0-08-102886-5.00005-0

Meng X, Cui X, Rajan NP, Yu L, Deng D, Bao X (2019) Direct Methane Conversion under mild Condition by Thermo-, Electro-, or Photocatalysis. Chem 5:2296–2325. https://doi.org/10.1016/j.chempr.2019.05.008

Montini T, Melchionna M, Monai M, Fornasiero P (2016) Fundamentals and Catalytic applications of CeO_2-Based materials. Chem Rev 116:5987–6041. https://doi.org/10.1021/acs.chemrev.5b00603

Mousavian P, Esrafili MD (2020) Methane oxidation into methanol catalyzed by TM-anchored $C_{24}N_{24}$ nanoclusters (TM = Fe, Co and Ni): a DFT study. Inorg. Chem Commun 122:108317. https://doi.org/10.1016/j.inoche.2020.108317

Niu J, Du X, Ran J, Wang R (2016) Dry (CO_2) reforming of methane over pt catalysts studied by DFT and kinetic modeling. Appl Surf Sci 376:79–90. https://doi.org/10.1016/j.apsusc.2016.01.212

Nolan M (2012) Charge transfer and formation of reduced Ce^{3+} upon adsorption of metal atoms at the ceria (110) surface. J Chem Phys 136:134703. https://doi.org/10.1063/1.3697485

Perdew JP, Burke K, Ernzerhof M (1996) Generalized gradient approximation made simple. Phys Rev Lett 77:3865. https://doi.org/10.1103/PhysRevLett.77.3865

Perdew JP, Ruzsinszky A, Csonka GI, Vydrov OA, Scuseria GE, Constantin LA, Zhou X, Burke K (2008) Restoring the density-gradient expansion for exchange in solids and surfaces. Phys Rev Lett 100:136406. https://doi.org/10.1103/PhysRevLett.100.136406

Qin YY, Su YQ (2021) A DFT study on heterogeneous Pt/CeO_2(110) single atom catalysts for CO oxidation. ChemCatChem 13:3857–3863. https://doi.org/10.1002/cctc.202100643

Qu P-F, Wang G-C (2022) DFT-based microkinetic model analysis of dry reforming of methane over Ru_7/CeO_2(111) and Ru_7/CeO_2(110): key role of surface lattice oxygen vacancy. Catal Sci Technol 12:1880–1891. https://doi.org/10.1039/D1CY01934A

Ravi M, Ranocchiari M, van Bokhoven JA (2017) The direct Catalytic Oxidation of methane to Methanol–A critical Assessment.

Angew Chem Int Ed 56:16464–16483. https://doi.org/10.1002/anie.201702550

Reddy KS, S V P, Deshpande PA (2022) DFT + U analysis of the stability of $Pd_n/CeO_{2-\delta}$ (n = 3,4). Appl Surf Sci 589:152948. https://doi.org/10.1016/j.apsusc.2022.152948

Riley C, Zhou S, Kunwar D, De La Riva A, Peterson E, Payne R, Gao L, Lin S, Guo H, Datye A (2018) Design of effective catalysts for selective Alkyne Hydrogenation by Doping of Ceria with a single-atom promotor. J Am Chem Soc 140:12964–12973. https://doi.org/10.1021/jacs.8b07789

Sedov I, Arutyunov V, Tsvetkov M, Podlesniy D, Salganskaya MV, Zaichenko A, Tsvetkova YY, Nikitin A, Ozerskii AV, Fokin IG, Salgansky EA (2022) Evaluation of the possibility to Use Coalbed Methane to produce methanol both by Direct Partial Oxidation and from Synthesis Gas. Eurasian Chem Technol J 24:157. https://doi.org/10.18321/ectj1328

Shi Y, Ma Z-R, Xiao Y-Y, Yin Y-C, Huang W-M, Huang Z-C, Zheng Y-Z, Mu F-Y, Huang R, Shi G-Y, Sun Y-Y, Xia X-H, Chen W (2021) Electronic metal–support interaction modulates single-atom platinum catalysis for hydrogen evolution reaction. Nat Commun 12:3021. https://doi.org/10.1038/s41467-021-23306-6

Singal CM, Das TP (1977) Electronic structure of ferromagnetic hcp cobalt. II. Cohesive energy and core exchange splittings. Phys Rev B 16:5093–5107. https://doi.org/10.1103/PhysRevB.16.5093

Singha RK, Tsuji Y, Mahyuddin MH, Yoshizawa K (2019) Methane activation at the metal-support interface of Ni_4-CeO_2(111) Catalyst: a theoretical study. J Phys Chem C 123:9788–9798. https://doi.org/10.1021/acs.jpcc.8b11973

Song W, Hensen EJM (2013) Structure sensitivity in CO Oxidation by a single au Atom supported on Ceria. J Phys Chem C 117:7721–7726. https://doi.org/10.1021/jp400977m

Strassner T, Ahrens S, Muehlhofer M, Munz D, Zeller A (2013) Cobalt-catalyzed oxidation of methane to Methyl Trifluoroacetate by Dioxygen. Eur J Inorg Chem 2013:3659–3663. https://doi.org/10.1002/ejic.201300213

Taylor SH, Hargreaves JSJ, Hutchings GJ, Joyner RW, Lembacher CW (1998) The partial oxidation of methane to methanol: an approach to catalyst design. Catal Today 42:217–224. https://doi.org/10.1016/S0920-5861(98)00095-9

Tian D, Zeng C, Wang H, Cheng X, Zheng Y, Xiang C, Wei Y, Li K, Zhu X (2017) Effect of transition metal fe adsorption on CeO_2(110) surface in the methane activation and oxygen vacancy formation: a density functional theory study. Appl Surf Sci 416:547–564. https://doi.org/10.1016/j.apsusc.2017.04.028

Tian D, Li K, Wei Y, Zhu X, Zeng C, Cheng X, Zheng Y, Wang H (2018) DFT insights into oxygen vacancy formation and CH_4 activation over CeO_2 surfaces modified by transition metals (Fe, Co and Ni). PCCP 20:11912–11929. https://doi.org/10.1039/c7cp08376a

Vayssilov GN, Lykhach Y, Migani A, Staudt T, Petrova GP, Tsud N, Skála T, Bruix A, Illas F, Prince KC, Matolı´n V r, Neyman K M, Libuda J (2011) Support nanostructure boosts oxygen transfer to catalytically active platinum nanoparticles. Nat Mater 10:310–315. https://doi.org/10.1038/nmat2976

Vovchok D, Guild CJ, Dissanayake S, Llorca J, Stavitski E, Liu Z, Palomino RM, Waluyo I, Li Y, Frenkel AI, Rodriguez JA, Suib SL, Senanayake SD (2018) In situ characterization of Mesoporous Co/CeO_2 catalysts for the high-temperature water-gas shift. J Phys Chem C 122:8998–9008. https://doi.org/10.1021/acs.jpcc.8b01271

Wei J, Iglesia E (2004) Isotopic and kinetic assessment of the mechanism of reactions of CH_4 with CO_2 or H_2O to form synthesis gas and carbon on nickel catalysts. J Catal 224:370–383. https://doi.org/10.1016/j.jcat.2004.02.032

Wu S, Wang Y, Cao Q, Zhao Q, Fang W (2021) Efficient imine formation by oxidative coupling at low temperature catalyzed by high-surface-area mesoporous CeO_2 with exceptional Redox Property. Chem-Eur J 27:3019–3028. https://doi.org/10.1002/chem.202003915

Wu S, Liu H, Huang Z, Xu H, Shen W (2022) O-vacancy-rich porous MnO_2 nanosheets as highly efficient catalysts for propane catalytic oxidation. Appl Catal B-Environ 312:121387. https://doi.org/10.1016/j.apcatb.2022.121387

Wu S, Liu H, Huang Z, Xu H, Shen W (2023) Mn1ZrxOy mixed oxides with abundant oxygen vacancies for propane catalytic oxidation: insights into the contribution of Zr doping. Chem Eng J 452:139341. https://doi.org/10.1016/j.cej.2022.139341

Xie K, Cheng F, Duan X (2021) Dry reforming of CH_4/CO_2 by stable ni nanocrystal on porous single-crystalline MgO monoliths at reduced temperatures. Angew Chem Int Ed 60:18792–18799. https://doi.org/10.1002/anie.202106243

Xu H, Chu W, Sun W, Jiang C, Liu Z (2016) DFT studies of Ni Cluster on graphene surface: effect of CO_2 activation. RSC Adv 6:96545–96553. https://doi.org/10.1039/C6RA14009B

Yang Y, Li T, Feng P, Wang X, Wang S, Ling Y, Shao Z (2022a) Highly efficient conversion of oxygen-bearing low concentration coal-bed methane into power via solid oxide fuel cell integrated with an activated catalyst-modified anode microchannel. Appl Energy 328:120134. https://doi.org/10.1016/j.apenergy.2022.120134

Yang Y, Liu Y, Chen Z, Li M, Rao M, Wang X, Feng P, Zhou F, Ling Y (2022b) Enhanced conversion efficiency and coking resistance of solid oxide fuel cells with vertical-microchannel anode fueled in CO_2 assisted low-concentration coal-bed methane. Sep Purif Technol 288:120665. https://doi.org/10.1016/j.seppur.2022.120665

Yang Q, Chen L, Jin N, Zhu Y, He J, Zhao P, Huang C, Wei L, Ma X, Wang X (2023) Boosted carbon resistance of ceria-hexaaluminate by in-situ formed $CeFe_xAl_{1-x}O_3$ as oxygen pool for chemical looping dry reforming of methane. Appl Catal B-Environ 330:122636. https://doi.org/10.1016/j.apcatb.2023.122636

Yoshida M, Tsuji Y, Iguchi S, Nishiguchi H, Yamanaka I, Abe H, Kamachi T, Yoshizawa K (2022) Toward computational screening of bimetallic alloys for methane activation: a Case Study of MgPt Alloy. ACS Catal 12:9458–9472. https://doi.org/10.1021/acscatal.2c01601

Zhang Q-H, Li Y, Xu B-Q (2004) Reforming of methane and coal-bed methane over nanocomposite Ni/ZrO_2 catalyst. Catal Today 98:601–605. https://doi.org/10.1016/j.cattod.2004.09.015

Zhang X, He D, Zhang Q, Xu B, Zhu Q (2005) Comparative studies on direct conversion of methane to methanol/formaldehyde over La–Co–O and ZrO_2 supported molybdenum oxide catalysts. Top Catal 32:215–223. https://doi.org/10.1007/s11244-005-2894-5

Zhang Q, Wu X-P, Li Y, Chai R, Zhao G, Wang C, Gong X-Q, Liu Y, Lu Y (2016) High-performance PdNi Nanoalloy Catalyst in situ structured on Ni Foam for Catalytic Deoxygenation of Coal-bed methane: experimental and DFT studies. ACS Catal 6:6236–6245. https://doi.org/10.1021/acscatal.6b01226

Zhang F, Liu Z, Zhang S, Akter N, Palomino RM, Vovchok D, Orozco I, Salazar D, Rodriguez JA, Llorca J, Lee J, Kim D, Xu W, Frenkel AI, Li Y, Kim T, Senanayake SD (2018) In situ elucidation of the active state of Co-CeO_x catalysts in the dry reforming of methane: the important role of the reducible oxide support and interactions with Cobalt. ACS Catal 8:3550–3560. https://doi.org/10.1021/acscatal.7b03640

Zhang Y, Song K, Cao S, Jian X, Qian P (2021) Density functional theory study of formaldehyde adsorption and decomposition on co-doped defective CeO_2(110) surface*. Chin Phys B 30:103101. https://doi.org/10.1088/1674-1056/abff42

Zheng C, Bu H, Yang F, Xu Z, Zhao H (2022) Size effect of $(CuO)_n$ (n = 1–6) clusters on the modification of Rutile-TiO_2 Photocatalysts. Energy Technol 10:2270011. https://doi.org/10.1002/ente.202270011

Zhou J, Du L, Braedt DL, Miao J, Senanayake SD (2021) Growth, sintering, and chemical states of Co supported on reducible $CeO_2(111)$ thin films: the effects of the metal coverage and the nature of the support. J Chem Phys 154:044704. https://doi.org/10.1063/5.0036952

Zhou S, Wan Q, Lin S, Guo H (2022) Acetylene hydrogenation catalyzed by bare and Ni doped $CeO_2(110)$: the role of frustrated Lewis pairs. https://doi.org/10.1039/D2CP00925K. PCCP